3D nickel electrodes for hybrid battery and electrolysis devices

Möller-Gulland, Robin; Mulder, Fokko M.

DOI
10.1016/j.xcrp.2024.102286

Publication date
2024

Document Version
Final published version

Published in
Cell Reports Physical Science

Cell Reports
Physical Science

CellPress
OPEN ACCESS

Article

3D nickel electrodes for hybrid battery and electrolysis devices

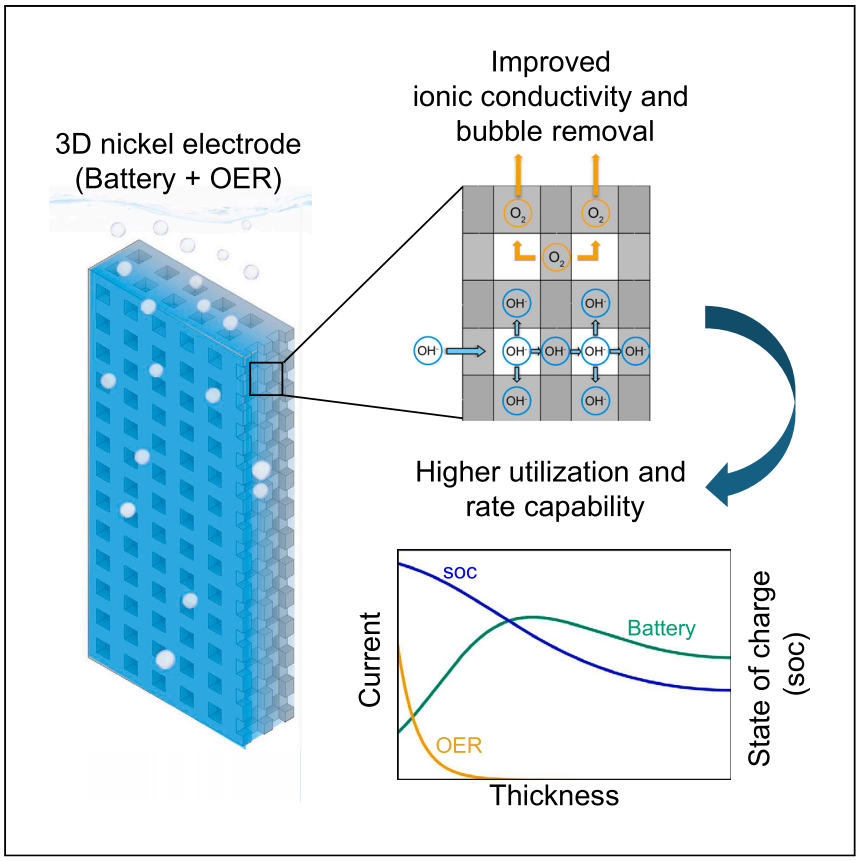

Möller-Gulland and Mulder demonstrate that an electrode design with 3D macroscopic channels in the microporous structure enables high charge, electrolysis, and discharge current densities in nickel hydroxide-based electrodes. This development brings forward fully flexible integrated Ni-Fe battery and alkaline electrolyzers, strengthening the individual applications while reducing the material footprints of both.

Robin Möller-Gulland, Fokko M. Mulder

f.m.mulder@tudelft.nl

Highlights

3D electrodes enable high current density (dis)charging of Ni-Fe battery electrodes

Charge rates reached are as high as alkaline electrolyzer current densities

Electrochemical modeling describes battery-electrolyzer charge utilization

3D structuring can be realized using scalable techniques

Möller-Gulland & Mulder, Cell Reports Physical Science 5, 102286
November 20, 2024
Published by Elsevier Inc.
https://doi.org/10.1016/j.xcrp.2024.102286

Cell Reports
Physical Science

CellPress
OPEN ACCESS

Article

3D nickel electrodes for hybrid battery and electrolysis devices

Robin Möller-Gulland[1] and Fokko M. Mulder[1,2,*]

SUMMARY

A renewable power-based energy system will require both short- and long-term electricity storage and conversion to hydrogen-based fuels. This study investigates 3D electrodes for an integrated alkaline Ni-Fe battery and electrolyzer. The dual system can sustain current densities similar to those in alkaline electrolyzers while simultaneously reaching efficient hour-duration battery-storage capacities. We demonstrate that the combination of microporosity and a conductive three-dimensional (3D) electrode design with macroscopic channels enables the required current densities during charge, electrolysis, and discharge. The ionic conduction in the 3D electrode enables higher utilization of the active electrode mass and lower overpotentials during both the (dis)charge reaction and electrolysis. The double function of these electrodes is understood from a general statistical model and a more detailed porous-electrode model perspective. The 3D structuring provides a pathway forward, accessible with industrially established techniques, to these higher-power and higher-energy-density electrodes.

INTRODUCTION

Climate change has been identified as one of the key dangers to our society.[1–3] Primarily driven by anthropogenic CO_2 emissions as a result of energy production from fossil fuels, the move to renewable, carbon-neutral energy sources is imperative in order to reach net zero CO_2 emissions by 2050 and limit global warming to 1.5°C.[3] Such energy sources include wind- and solar-generated power with intrinsic seasonal and daily variations in output. To allow for a continuous energy supply and to stabilize the electrical grid, large-scale energy-storage solutions are necessary on short daily and long seasonal timescales.[4,5] These include battery-storage technologies as well as energy storage in the form of synthetic renewable fuels such as H_2 or NH_3. With round-trip energy efficiencies as high as 90%, batteries are an attractive solution for diurnal, short-term energy storage. However, batteries are only of limited use for seasonal, long-term energy storage (i.e., months, years). This is due to the high cost of large-scale battery-storage facilities that requires as many charge and discharge cycles over a year as possible to obtain a reduced cost per storage cycle; one cycle per year as seasonal storage makes batteries economically unattractive for this application. An energy carrier such as H_2, on the other hand, can be stored externally after being produced, which makes it a good option for long-term energy storage. However, the overall electrical efficiency of energy storage in the form of hydrogen is low, as it includes both the production via electrolysis and the recuperation into electricity, for example via a fuel cell or a gas turbine. As a result, batteries as well as both H_2 and H_2-derived fuels are expected to complement each other in the future energy-storage infrastructure.[6] In addition, H_2 is

[1]Materials for Energy Conversion and Storage (MECS), Delft University of Technology, 2629 HZ Delft, the Netherlands

[2]Lead contact

*Correspondence: f.m.mulder@tudelft.nl

https://doi.org/10.1016/j.xcrp.2024.102286

an important feedstock for the chemical industry, but its production from renewable power preferably only occurs when there is more green power than required for all other applications, and one is not firing up a gas-fired powered power plant—on H_2—to generate electricity at the same time. Such H_2 feedstock generation thus occurs necessarily at a lower utilization or capacity factor than is applied currently with fossil H_2 generation.

A recent approach developed in our group is the development of a hybrid battery and alkaline electrolyzer (Battolyser^{TM}).[7] In this concept, a nickel-iron battery functions as an alkaline electrolyzer to produce H_2 and O_2 when overcharged and can be discharged after electrolysis operation. The negative electrode is based on $Fe(OH)_2$ as active material that is reduced to Fe upon charge (Fe charge reaction, −0.88 V vs. standard hydrogen electrode [SHE]):

$$Fe(OH)_2 + 2e^- \underset{\text{discharging}}{\overset{\text{charging}}{\rightleftharpoons}} Fe + 2OH^-. \quad \text{(Equation 1)}$$

The positive electrode is based on $Ni(OH)_2$ as active material that releases a proton and electron during the charge reaction (CR, +0.49 V vs. SHE):

$$Ni(OH)_2 + OH^- \underset{\text{discharging}}{\overset{\text{charging}}{\rightleftharpoons}} NiOOH + H_2O + e^-. \quad \text{(Equation 2)}$$

The OH^- ions are conducted by an aqueous alkaline KOH electrolyte. During charging, Fe and NiOOH become increasingly present and function as efficient HER and oxygen evolution reaction (OER) catalysts, respectively. As a result, the electrochemical reaction shifts from the battery-charging reaction to electrolysis. Hydrogen evolution takes place at the negative iron electrode (HER, −0.861 V vs. SHE at pH 14.6):

$$2H_2O + 2e^- \xrightarrow{\text{overcharging}} H_2(g) + 2OH^-, \quad \text{(Equation 3)}$$

while oxygen is generated at the positive nickel electrode (OER, +0.369 V vs. SHE at pH 14.6):

$$4OH^- \xrightarrow{\text{overcharging}} O_2(g) + H_2O + 4e^-. \quad \text{(Equation 4)}$$

Thus, both energy-efficient short-term battery storage and long-term energy storage are integrated in a single device, which reduces cost and increases the utilization factor overall, while accommodating a lower utilization factor for either functionality alone. Moreover, the main materials required for nickel-iron (Ni-Fe) batteries count among the most abundant elements in the earth's crust. The first prototype developed by Mulder et al.[7] employed commercial-type nickel and iron pocket electrodes. It showed that double functionality enhanced the utilization of the full battery capacity, mainly due to charging continuing while gas evolution also starts. Also, high efficiencies were observed at 82%–90% combined battery round-trip efficiency and H_2 generation (with respect to the higher heating value [HHV] of hydrogen). Long-term cycling results indicate the feasibility of the approach. In conventional Ni-Fe batteries, gas evolution due to electrolysis has been considered a parasitic side reaction that increases self-discharge and reduces the charging efficiency.[8,9] The latter is adversely impacted by, and thus limits, high charge rates.[10] For this reason, suppressing OER and HER by means of additives in the active material and electrolyte has been a major focus in past battery electrode development.[11–14] However, when the water splitting adds useful product, these additives are no longer necessary, opening the possibility to optimize both battery and electrolysis activity. An example is replacing Co dopants in $Ni(OH)_2$ meant to suppress OER

by Fe to promote OER, while remarkably also increasing the battery-storage capacity.[15] Also, the current densities applied in alkaline electrolysis reach about 200–240 mA/cm^2 for non-noble catalyst Ni-based systems at 80% efficiency (with respect to the HHV of hydrogen).[16,17] Higher current densities require noble-metal-catalyst-promoted electrodes and zero-gap designs to reduce ohmic resistances. However, the latter come at the cost of enhanced gas crossover and, therefore, minimal power requirements, i.e., reduced operational flexibility.[18,19]

As indicated by Mulder[4] and the TenneT TSO Adequacy Outlook report,[20] the typical installed capacity of battery storage and electrolysis (power to gas) capacity is roughly similar on a future large gigawatt-scale system level. In addition, the battery storage needs to be able to store at this power for about 4 h. The combined battery and electrolysis capacity then becomes proportional to 1 GW + 1 GW = 2 GW and 4 GWh. Taking this as a possible reference target, one would therefore be interested in C/2 charge rates and C/4 discharge rates of an integrated battery-electrolyzer system to support the fully renewables-based electricity system by 2050. Such can then be applied for approximately 4–6 h of daily overproduction; during such periods of low electricity prices, the combined battery-electrolyzer is first charged and subsequently produces H_2 at low cost, which can be used as chemical feedstock or for long-term energy storage. In the following 4–10 h of renewable underproduction, the battery can be discharged at anticipated higher electricity price (C/4 to C/10 discharge rate). An illustration of such a charge/discharge scheme is given in Figure S1, synchronized with the Dutch Day Ahead Market of April 19, September 19, and September 20, 2023. In addition to such diurnal battery and long-term H_2 energy storage, short-term energy arbitrage and grid-stabilization services such as frequency regulation and voltage support may require higher charge and discharge rates to respond effectively to rapid changes in grid conditions and capitalize on fluctuations in energy prices. To allow for more flexible power use, one can therefore also target a 1 C charge rate and C/4 discharge rates, while the charge rate is also reaching similar current densities as state-of-the-art, non-noble-metal-catalyzed, alkaline electrolyzers. The target could then become ~200 mA/cm^2 and ~200 mAh/cm^2 at 1 C charge and C/4 discharge.

The electrodes in commercial Ni-Fe batteries are not designed to facilitate these high current densities and typically only have rated capacities below 50–80 mAh/cm^2 at C/4 or C/10 discharge rates.[7,21] In pocket-type electrodes the active material and conductive additives are pressed and enclosed in perforated steel pockets. While these can be produced at low cost, material utilization at higher charge and discharge rates is limited by the poor electronic conductivity provided by the contact between dispersed particles of active material and conductive additives (e.g., carbon, nickel powder). Sintered electrodes, on the other hand, are made by fusing (sintering) metal particles at high temperatures resulting in highly porous, conductive metal substrates with high surface area. These properties allow for significantly higher charge and discharge rates as well as improved active material utilization compared to pocket-type electrodes. However, Lim and Verzwyvelt[10] demonstrated sintered nickel electrodes with rated capacities as high as 130 mAh/cm^2 that were charged with current densities of up to 260 mA/cm^2 but returned a limited 44% material utilization (1.3 C charge insertion, 73 mAh/cm^2 charged capacity). Even though sintered electrodes offer significant improvements in rate capability, their thickness, and therefore their capacity, is still limited by the effective ionic conductivity within the electrode. As a result, active material farthest from the front of the electrode is utilized the least, so that increasing the electrode thickness only yields diminishing returns in capacity increase.[10,22] The effective

thickness or areal capacity, however, is essential for increasing the energy density of the system by increasing the ratio of active material over inactive separator, current collector, and electrolyte materials in the cell while maintaining good transport properties.[23] Due to the comparatively high cost, sintered electrodes are therefore kept thin (<1 mm) and applied in applications where power density is prioritized over energy density. Furthermore, electrolysis, i.e., overcharging, at the targeted current densities requires the effective removal of H_2 and O_2 bubbles from the electrode and cell. These reduce the effective electrolyte conductivity and shield electrochemically active sites, resulting in an increase in cell potential.[24,25]

Overall, it is clear that the development of future integrated battery-electrolyzer systems requires novel electrodes and cell concepts specifically designed for this hybrid application. In recent years, three-dimensional (3D) electrodes have been demonstrated successfully for use in electrochemical applications, where the electrode geometry presents an additional degree of freedom in electrode development.[26–28] 3D flow-through electrodes have been shown to improve mass transfer in electrochemical reactors[29–33] and facilitate bubble removal in alkaline electrolysis.[34–36] Saleh et al.[37] reported how 3D hierarchically porous microlattice electrodes for Li-ion batteries increase electrolyte accessibility and available electrochemically active surface area, resulting in a 100% increase in areal capacity. 3D-printed lithium-ion battery electrodes have been shown to be capable of reaching 10 mAh/cm^2,[38] and 3D electrodes have also been demonstrated for lightweight Ni-Fe batteries for the use in smart devices and wearable electronics.[39,40] However, with areal capacities of around 10 mAh/cm^2, these are more than an order of magnitude below the application targeted in this work. Furthermore, Kou et al.[35] highlighted the benefits of an ordered channel structure of a 3D electrode for the removal of O_2 bubbles during electrolysis as compared to stochastically structured nickel foam electrodes.

Due to the benefits of 3D electrodes shown for both battery and electrolysis applications, we hypothesized that such open and ordered structures should also improve the performance of hybrid battery-electrolysis electrodes. Here, we report the development of a 3D hierarchically porous sintered nickel electrode with a high areal capacity of 140 mAh/cm^2 that facilitates rapid bubble release and increases the ionic conductivity within the electrode. Compared to a non-3D-structured conventional electrode geometry, this results in decreased overpotentials, high materials utilization, and significantly improved rate capability approaching current densities of industrial alkaline electrolyzers. Using a porous-electrode model, we show how this boost in performance is the result of a more homogeneous current distribution throughout the 3D electrode. The designed 3D structure effectively channels the ionic current deeper into the electrode than without the 3D structure, a result in line with a porous-electrode optimization approach of Roy et al.[41] From this proof of concept the electrode geometry can be adjusted to allow for large-scale manufacturing using powder metallurgy processes such as press-and-sinter and metal injection molding.[42–44]

RESULTS AND DISCUSSION

Dual-function electrode

To understand the interplay of battery charging and electrolysis, a simple statistical approach for describing the state of charge $S(q)$ as a function of inserted charge q is insightful. Assume the nickel electrode is limiting (oversized iron electrode) and the fraction of uncharged $Ni(OH)_2$ material is equal to $(1 - S(q))$ and that conductivities

are ideal, so there are no effects of potential distribution. Upon charge insertion, the material will be charged according to Equation 2 and increase its $S_{\text{unchgarged}}(q)$ as

$$dS_{\text{uncharged}}(q) = (1 - S(q))dq. \quad \text{(Equation 5)}$$

However, the fraction $S(q)$ that is already charged can perform two electrochemical activities: it can oxidize water to form O_2 as in Equation 4 or it can charge connected material further with a probability $(1 - S(q))$. The increase of $S_{\text{charged}}(q)$ when inserting a charge dq then becomes

$$dS_{\text{charged}}(q) = S(q)(1 - S(q))dq. \quad \text{(Equation 6)}$$

The total change in dS then becomes

$$\begin{aligned} dS(q) &= dS_{\text{uncharged}}(q) + dS_{\text{charged}}(q) = (1 - S(q))dq \\ &+ S(q)(1 - S(q))dq = (1 - S^2(q))dq, \end{aligned} \quad \text{(Equation 7)}$$

the solution of which is

$$S(q) = \tan h(q), 0 \leq q \leq \infty. \quad \text{(Equation 8)}$$

Note that Equation 7 can be rewritten as $dS(q)/dq = 1 - S^2(q) = 1 - tanh^2(q) = I_{CR}(q)/I_{\text{ch}}$, which indicates how much of the total inserted charge I_{ch} is spent on CR while the OER consumes $S^2(q)$.

Remarkably, this charge retention Equation 8 for $S(q)$ is the same as the observed "logistic equation" (9) in our previous work.[7] The description immediately indicates how the electrode can accommodate the two competing reactions 2 and 4. However, when applying higher current densities or thick electrodes, the resistances, transport phenomena, and activation potentials do become a factor of importance, and the electrochemistry occurs progressively more at the electrode side closest to the counter electrode. The random statistical aspect is then an oversimplification, and a more detailed porous-electrode model is required in which the current distribution across the electrode thickness as well as reaction kinetics are considered. A limited description of this model is described below. A more detailed description will be provided in a future publication.

Porous-electrode model

To assess how the 3D structure affects both battery charging and OER performance, we studied the current and potential distribution using a simplified porous-electrode model. A 3D electrode consists of sintered porous-electrode material interspersed with open volumes (e.g., channels) filled with electrolyte. As a result, we define two types of porosity (Figure 1): the microscopic porosity of the electrode material, ϵ, and the macroscopic porosity or void fraction, Θ, that describes the ratio of the open volume to the geometric volume of the electrode (V_{el}). In a 3D electrode Θ can vary in all three spatial dimensions depending on the specific features of the electrode geometry. Therefore, an electrode model developed for a specific geometry can be complex to implement and computationally expensive. To arrive at a more general one-dimensional (1D) model, we describe the electrode using effective medium theory where we assume average values for properties such as void fraction, material porosity, and surface area throughout the electrode. This allows us to define an effective electrolyte conductivity within the electrode:

$$\kappa_{\text{eff,3D}} = \kappa[(1 - \Theta)\epsilon^{\tau} + \Theta], \quad \text{(Equation 9)}$$

where κ is the bulk electrolyte conductivity and τ represents the tortuosity of the pores in the electrode substrate. For a conventional non-3D structured electrode with $\Theta = 0$, Equation 9 reduces to Bruggeman's equation commonly used in 1D

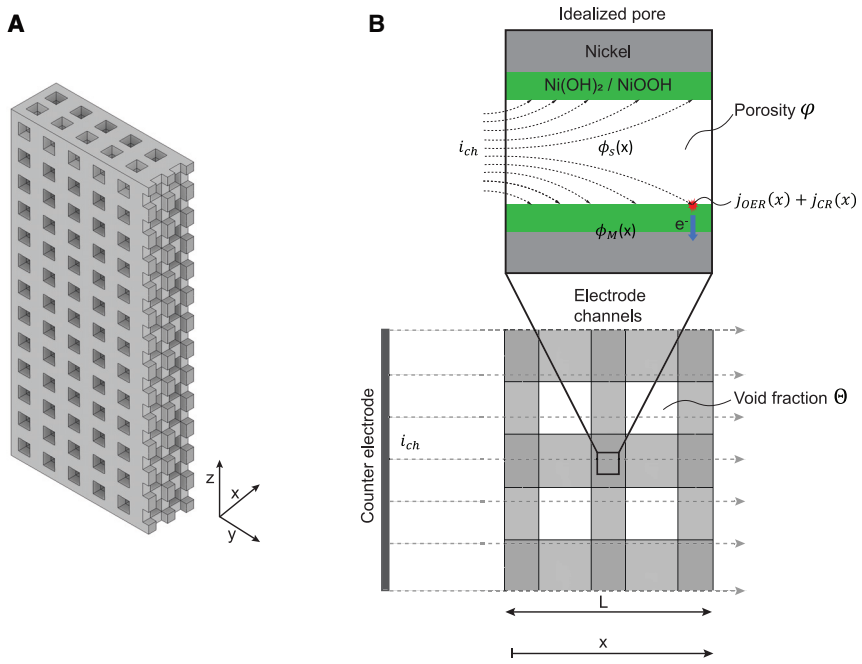

Figure 1. Schematic of a porous 3D electrode

(A) Cross-section of a 3D electrode showing channels in x, y, and z directions.

(B) Representation of potentials and reactions in the idealized porous sintered nickel structure with micron-scale porosity ϕ and the electrode channels constituting the macroscopic void fraction Θ.

electrode models.[45] Since the goal of this model is a first assessment of the impact of a 3D structure on the current and potential distribution, we simplify the model further by assuming that the reactant concentration in the electrolyte remains constant over time and throughout the electrode. Moreover, we do not take effects of bubbles on the electrolyte conductivity and surface coverage into account. Assuming electroneutrality and neglecting double-layer charging, a charge balance in the electrolyte yields

$$\frac{d^2\phi_S(x)}{x^2} = -\frac{a_0(1-\Theta)}{\kappa_{eff,3D}}(j_{OER}(x) + j_{CR}(x)). \quad \text{(Equation 10)}$$

Here, $\phi_S(x)$ represents the electrolyte potential, a_0 is the volume-specific electrochemically active surface area of a conventional non-3D electrode, and $j_{OER}(x)$ and $j_{CR}(x)$ correspond to the local current densities for the OER and battery-charging reaction, respectively. Ta and Newman determined that the exchange current density for oxygen evolution on pure nickel hydroxide films increases linearly with the state of charge *soc* and exhibits irreversible Tafel behavior, so that $j_{OER}(x)$ can be expressed as[46]

$$j_{OER}(x) = j_{0,ref,OER}\left(\frac{c_{OH}}{c_{OH,ref}}\right)^2 soc(x)\exp\left(\frac{\alpha_{a,OER}F}{RT}\eta_{OER}(x)\right). \quad \text{(Equation 11)}$$

For the battery-charging reaction, we adapt the kinetic expression used by De Vidts and White[47] and Fan and White[48]:

$$j_{CR}(x) = 2j_{0,ref,CR}\left[\frac{c_{OH}}{c_{OH,ref}}(1-soc(x))\exp\left(\frac{\alpha_{a,CR}F}{RT}\eta_{CR}(x)\right) - soc(x)\exp\left(-\frac{\alpha_{c,CR}F}{RT}\eta_{CR}(x)\right)\right]. \quad \text{(Equation 12)}$$

In the equations above, $j_{0,ref}$, α_a, and α_c represent the exchange current density as well as the anodic and cathodic transfer coefficients, respectively, for the OER and CR reactions measured at the reference hydroxide concentration $c_{OH,ref}$. The local overpotentials $\eta_{OER}(x)$ and $\eta_{CR}(x)$ are given by

$$\eta_{OER}(x) = \phi_M - \phi_S(x) - E_{0,OER}, \quad \text{(Equation 13)}$$

$$\eta_{CR}(x) = \phi_M - \phi_S(x) - E_{0,CR}(x), \quad \text{(Equation 14)}$$

where $E_{0,OER}$ and $E_{0,CR}$ are the equilibrium potentials for the oxygen evolution and battery-charging reaction, respectively. $E_{0,CR}$ is known to be a function of the state of charge, which is described in more detail in Figure S4. Due to its high electronic conductivity, we assume that there is no gradient in the potential ϕ_M of the sintered nickel substrate. Equations 11, 12, and 14 require the calculation of the local state of charge which depends not only on the local charging current j_{CR} but also on the duration of charging. Therefore, the charge balance described in Equation 10 is implicitly a function of time. As we neglect double-layer charging and assume no changes in electrolyte composition, the potential and current profiles are formed instantaneously. In addition, we neglect mass transfer resistances within the $Ni(OH)_2$/NiOOH film and assume homogeneous charging throughout its thickness. As a result, Equation 10 describes the steady state of the potential and current distribution at a time t. The local state of charge (soc) after a time step Δt is then calculated as

$$soc(x, t + \Delta t) = soc(x, t) + \frac{V_{el} a_0 (1 - \Theta) j_{CR}(x)}{C} \Delta t, \quad \text{(Equation 15)}$$

which is used to determine the potential and current distribution at the time $t + \Delta t$. Here, C refers to the total battery capacity of the electrode. The overall state of charge of the electrode (SOC) is defined as

$$SOC\ (t + \Delta t) = \frac{1}{L} \int_0^L soc\ (x, t + \Delta t)\ dx, \quad \text{(Equation 16)}$$

where L is the electrode thickness. The boundary conditions to solve Equation 10 are

$$\left. \frac{d\phi_S}{dx} \right|_{x = 0} = \kappa_{eff,3D}\ i_{ch}, \quad \text{(Equation 17)}$$

$$\left. \frac{d\phi_S}{dx} \right|_{x = L} = 0, \quad \text{(Equation 18)}$$

where i_{ch} is the geometric current density. The model described above allows for the estimate of the current distribution and local overpotentials for both CR and OER during charging and electrolysis. As a result, it can support our understanding of how the increased effective ionic conductivity of an open 3D electrode affects performance metrics such as material utilization and rechargeability at high charge rates. Notably, the electrode geometry is taken into account via the void fraction irrespective of the specific features of the geometry (Equation 9). Therefore, the model can be used in a fast assessment of these main parameters in the 3D electrode geometries without considering a specific shape in more complex 3D models than required as long as bubble removal and mass transfer is possible.

Electrode preparation

The electrodes serving here as prototype were prepared using the technique of indirect 3D printing introduced by Hereijgers et al.[30] and illustrated in

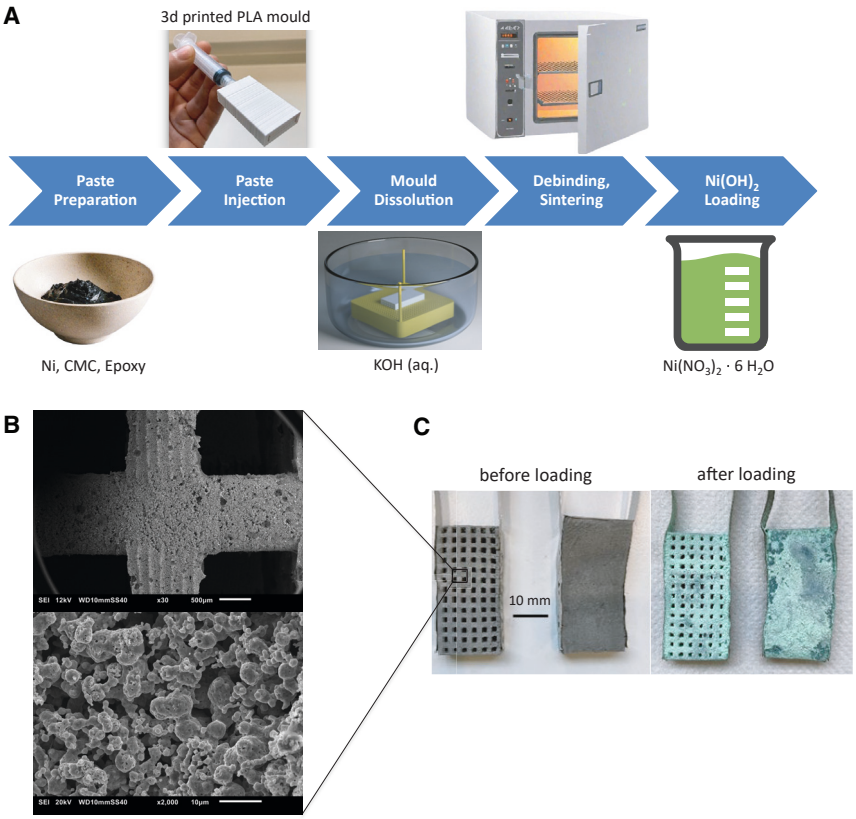

Figure 2. Indirect 3D printing and active material loading

(A) Schematic of the indirect 3D-printing procedure followed by active material loading via thermal decomposition of nickel nitrate hexahydrate.

(B) SEM images of a sintered 3D electrode before active material loading at 30× and 2,000× magnification. Scale bars, 500 μm (top) and 10 μm (bottom).

(C) 3D and non-3D electrode with spot-welded contacts before and after active material loading. Scale bar, 10 mm.

Figures 2 and S2. In essence, this technique involves 3D printing of a polymer mold of the electrode, which is then filled with a slurry containing the metal powder, a liquefying agent, and a binder. Following the hardening of the binder, the mold is removed by dissolution in a suitable solvent, which yields the green part of the electrode. The green part is then debinded and sintered to yield a mechanically stable, porous, and electronically conductive 3D electrode substrate. Building on the methodology of Hereijgers et al.,[30] we find that polylactic acid (PLA), a commonly used and cost-efficient fused deposition modeling (FDM) printing material, can be used as mold material that can be removed with a concentrated potassium hydroxide solution (30 wt % KOH(aq.)) (see Note S1). 3D electrode substrates manufactured with this technique exhibit porosities ranging from 70% to 80%. Such high porosities are required for the loading of $Ni(OH)_2$, which constitutes the active battery material and, when charged to NiOOH, catalyzes OER. To assess the effectiveness of a 3D electrode for the hybrid application as battery and oxygen evolution electrode, we prepared a 3D electrode with a void fraction of 40% and a conventional non-3D structured electrode as a control. Each electrode was loaded with $Ni(OH)_2$ to an area-specific capacity of approximately 140 mAh/cm^2 (Figures S3, S10, S14, and S15).

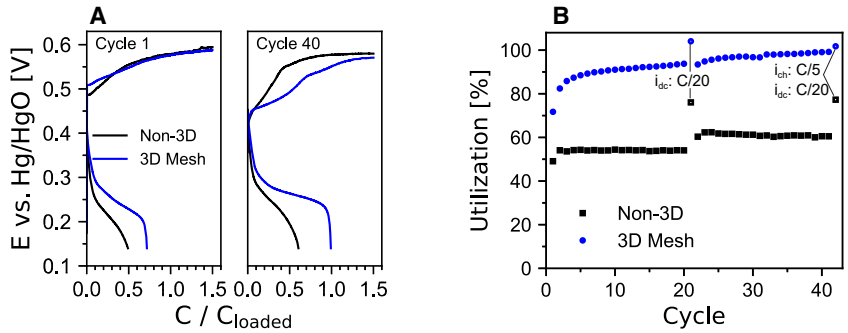

Figure 3. Activation cycles for the 3D mesh electrode and non-3D electrode

(A) Comparison of electrode potentials for activation cycles 1 and 40. Electrodes were overcharged by 50% at a charge rate of 1 C and a discharge rate of C/2.

(B) Active material capacity utilization over the 42 activation cycles with respect to the theoretical capacity of 289 mAh/g for the $Ni(OH)_2$/NiOOH redox couple. The discharge rate (i_{dc}) was reduced to C/20 in cycles 21 and 42. In cycle 42 the charge rate (i_{ch}) was reduced to C/5.

Electrode activation and battery-charging efficiency

The loaded active mass requires electrochemical activation before reaching its maximum discharge capacity.[49] Nickel electrode activation typically consists of charging and discharging cycles during which the electrode capacity gradually increases. Ideally, the time required for the activation procedure should be as short as possible so that the electrode operates sooner to specification. This is especially relevant for the nickel electrode, as it limits the battery capacity in a full cell. For batteries, (dis)charge rates and the inserted charge are typically expressed relative to a reference capacity. Here, we use the theoretical capacity of the loaded active material as reference (140 mAh/cm^2). For example, a charge rate of C/n (140/n mA/cm^2) indicates that inserting the charge of 1 C (140 mAh/cm^2) takes n hours. We define the utilization of the active material as the ratio of the discharge capacity C_{dc} to the theoretical capacity of the loaded active material C_{loaded}. The as-prepared electrodes were activated via the protocol described in Figure 3. A 1 C charge rate was utilized, since this is already faster than the C/2 rate indicated above as target for a full-scale system. As shown in Figure 3B, the 3D mesh electrode is activated far more effectively and reaches a utilization of over 90% after only eight activation cycles compared to 54% for the non-3D electrode. For further activation cycles, the discharge capacity of the 3D electrode increases steadily and eventually results in almost full utilization of the active material at the 1 C charge and C/2 discharge rate (cycle 41). The non-3D electrode, on the other hand, exhibits no further increase in discharge capacity until the discharge rate is decreased by a factor of 10 to C/20 (20 h discharge rate, cycle 21). It appears that a slow discharge rate allows for increased material accessibility, which facilitates activation. Interestingly, following this slow discharge, the utilization of the non-3D electrode is increased to 60% at the initial 1 C charge and C/2 discharge rate, yet does not increase further. This suggests that, in contrast to the 3D electrode, the active material of the non-3D electrode is only partially accessible at the C/2 discharge rate, resulting in incomplete cycling and activation. A further factor affecting material utilization is the battery-charging efficiency, which describes the ratio of the inserted charge going toward the battery-charging reaction CR as opposed to the competing OER. Whether CR or OER is dominant depends on kinetic parameters such as the anodic transfer coefficient and exchange current density, the state of charge, as well as the overpotentials for the respective reactions (Equations 11, 12, 13, and 14). At the beginning of charging, CR is favored due to the many orders of magnitude higher exchange current compared to that of OER. With an increase in

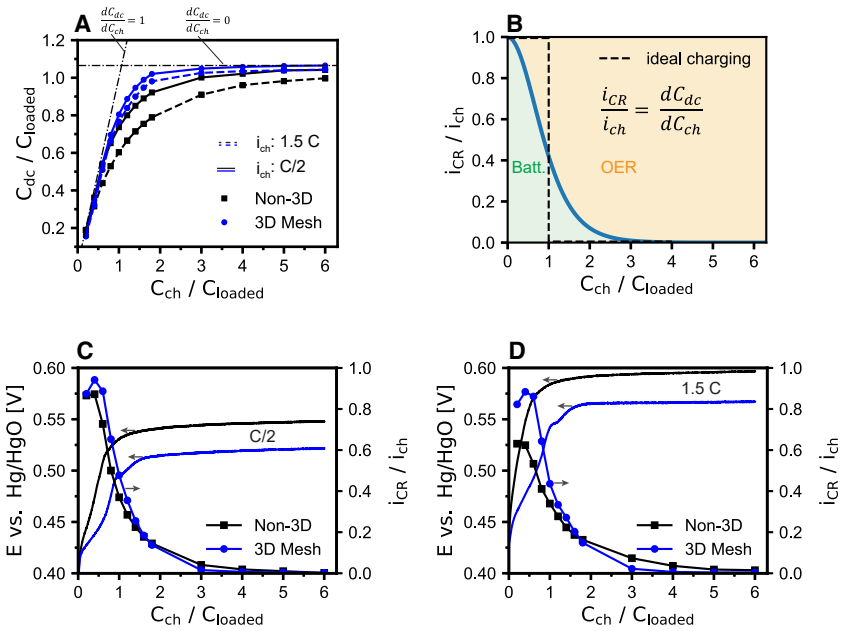

Figure 4. Charge retention and impact of oxygen evolution on battery capacity during charging

(A) Discharge capacity over charge insertion for charge rates of 0.5 C and 1.5 C and a constant discharge rate of C/4.

(B) Schematic of the shift in partial current for battery charging in the course of charging and overcharging (This behavior is described by Equations 8 and 19, $1 - tanh^2(x)$. Ideal charging would be a step function.

(C and D) Experimentally determined partial current for battery charging at C/2 and 1.5 C overlaid with voltage progression during charging and overcharging to 6 C. The arrows indicate the respective y axes for each curve.

state of charge, however, the anodic term in Equation 12 decreases and approaches zero when fully charged. In addition, the equilibrium potential $E_{0,CR}$ increases, which results in a reduced overpotential for CR (Figure S4). As a result, the dominant electrode reaction shifts from CR to OER in the course of charging. However, even at a lower state of charge the significantly lower equilibrium potential $E_{0,OER}$, and at elevated electrode polarization $\phi_M - \phi_S$, overpotentials for OER can become sufficiently high to cause a substantial OER current and reduction in charging efficiency. For this reason, a low charging potential is indicative of a high charging efficiency.

A common approach to increase the charging efficiency of nickel battery electrodes is to increase the OER potential by the addition of Co, Cd, or Ca in the $Ni(OH)_2$ in combination with LiOH in the electrolyte.[12,50,51] For a hybrid electrode, however, this suppression of OER is not required any longer, as water splitting is an intended product. In addition, as can be seen in Figure 3A, the average charging potential of the 3D electrode decreases noticeably during activation and is about 30 mV lower compared to that of the non-3D electrode in the final activation cycle at the 1 C charge rate. Therefore, the high utilization and more effective activation of the 3D electrode is now also the result of decreased overpotential and increase in charging efficiency, without the use of OER-suppressing additives.

The charging efficiency i_{CR}/i_{ch} can be estimated experimentally by inserting an increasing amount of charge and then measuring the discharge capacity after each charge insertion C_{ch} (Figure 4A). The discharge rate is kept sufficiently low at

C/4 to allow for the full discharge of the charged material, while the charge rate is varied in order to assess its impact on the charging efficiency. The charging efficiency can then be estimated as the rate of the increase of the discharge capacity when increasing the inserted charge (Figures 4C and 4D):

$$\frac{i_{CR}}{i_{ch}} = \frac{dC_{dc}}{dC_{ch}} \approx \frac{dS}{dq}. \quad \text{(Equation 19)}$$

Ideal charging describes the hypothetical case where OER only occurs after all of the active material is fully charged. However, as mentioned above, OER will already occur earlier. In this case, all the inserted current is initially spent on the CR, but above 2 C charge insertion the charging efficiency decreases to close to zero (Figure 4B). A high charging efficiency is not only beneficial for nickel battery electrodes but also for the operation of the hybrid electrodes presented here. Fast charging early on in the charging and electrolysis cycle allows for more flexible operation such as intermittent charge and discharge in response to electricity prices. As shown in Figures 4C and 4D, OER already occurs at the beginning of charging for both the 3D and non-3D electrode and is exacerbated by an increase in charge rate. For the tested charge rates of C/2 and 1.5 C, the 3D electrode exhibits higher charging efficiencies, so that OER is shifted toward the end of charging. As a result, a charge insertion of 1 C at the C/2 rate is sufficient to charge 80% of the loaded active material of the 3D electrode vs. 74% for the non-3D electrode. Remarkably, for a 3-fold increase in charging current (1.5 C), this value only decreases to 77% for the 3D electrode as opposed to 60% for the non-3D electrode, which exhibits a low initial charging efficiency of 60% (Figures 4A–4D). As shown for electrode activation (Figure 3A), the differences in charging efficiency are again reflected in the charging potentials (Figures 4C and 4D). These increase for higher charge rates and are considerably lower for the 3D electrode that shows about 50 mV reduction in the average charging potential for the 1.5 C charge rate. Since both electrodes have been loaded with the same active material and loading procedure, the observed increase in charging efficiency must be the result of the more open electrode structure.

How the electrode structure can have such a significant impact on the faradic charging efficiency becomes clear when considering the current distribution within the electrode throughout charging as determined using the porous-electrode model described above (Equations 9, 10, 11, 12, 13, 14, 15, 16, 17, and 18). These are shown in Figure 5A for different levels of charge insertion, where $\xi = x/L$ is the position x divided by the electrode thickness L. Whether OER or CR occurs at a depth x in the electrode depends on the local state of charge and the local overpotentials for the respective reactions. Since the exchange current density for CR is orders of magnitude higher than for OER, CR is dominant if the local state of charge is low and the overpotential for OER is sufficiently small compared to that of CR. The solution potential of the electrolyte and, therefore, the overpotentials of the respective reactions η_{CR} and η_{OER}, decrease exponentially over the electrode thickness as a consequence of the effective ionic resistance of the electrolyte within the electrode. Therefore, at the beginning of charging, the magnitude of the CR current density is highest at the front of the electrode with only negligible OER (Figure 5A). Here, the state of charge increases the fastest, resulting in the gradual transition from CR to OER. Charging continues within the electrode across a reaction front moving from the front to the back of the electrode. Comparing the current distribution of the 3D with those of the non-3D electrode, two observations stand out: first, at the beginning of charging, the battery-charging current density j_{CR} is distributed more homogeneously over the 3D electrode, resulting in a more homogeneous increase in state of charge. As a result, the onset of OER at the front of the electrode is

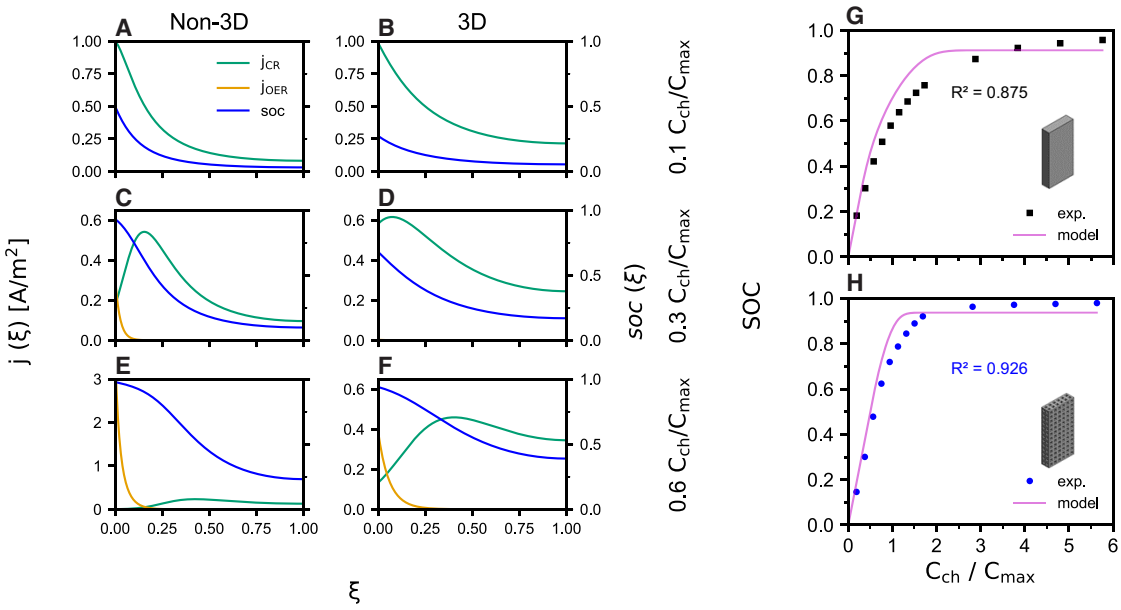

Figure 5. Modeled current distribution and charging efficiency throughout battery charging at a charge rate of 1.5 C

(A–F) Local state of charge (SOC) and current densities for oxygen evolution (j_{OER}) and battery-charging reaction (j_{CR}) across the reduced electrode thickness $\xi = x/L$ for increasing charge insertion C_{ch}. C_{max} refers to the maximum measured discharge capacity obtained for overcharging as shown in Figure 4A at C/2.

(G and H) Comparison of modeled overall state of charge (SOC) with experimental data for the 3D electrode (G) and non-3D electrode (H). The experimental SOC is determined from the discharge capacities shown in Figure 4A divided by C_{max}.

delayed. Second, even when OER increases at the front of the 3D electrode, CR continues with a current density of a comparable order of magnitude across its thickness. Overall, this increased homogeneity of the current distribution significantly improves (re)chargeability and is the direct result of the higher effective electrolyte conductivity, i.e., lower ionic resistance, provided by the electrode channels (9). Comparison with the experimental data shows that the simple porous-electrode model can qualitatively describe the charging behavior for the electrodes of varying void fraction at the 1.5 C charge rate discussed here (Figure 5). We find that the model overestimates the charging efficiency up to approximately 3 C charge insertion. This is possibly due to the simplifying assumptions made that neglect effects such as proton and charge transfer resistances within the active material as well as the reduction of surface area and electrolyte conductivity due to O_2 bubbles. Interestingly, the full capacity is not reached in the model for 3D nor non-3D electrode, but the 3D comes closer. This is due to Equation 12 approaching zero when the anodic term reduces and the cathodic term increases when the state of charge approaches 1.

High-rate battery performance

Hybrid battery-electrolyzer electrodes should provide a high charging efficiency and discharge capacity as well as sufficiently low overpotentials at increased charge and discharge rates. Figure 6 shows the impact of charge and discharge rates on discharge capacities and overpotentials for the 3D and non-3D electrode. Increasing the charge rate from C/10 to C/2 results in no significant decrease in discharge capacity of the non-3D electrode. Interestingly, the discharge capacity of the 3D mesh electrode increases up to a charge rate of 1 C. Higher charge rates are known to increase the attainable oxidation state of the active material.[50] If the charge rate is still sufficiently low to limit OER, this increased oxidation state results in higher discharge

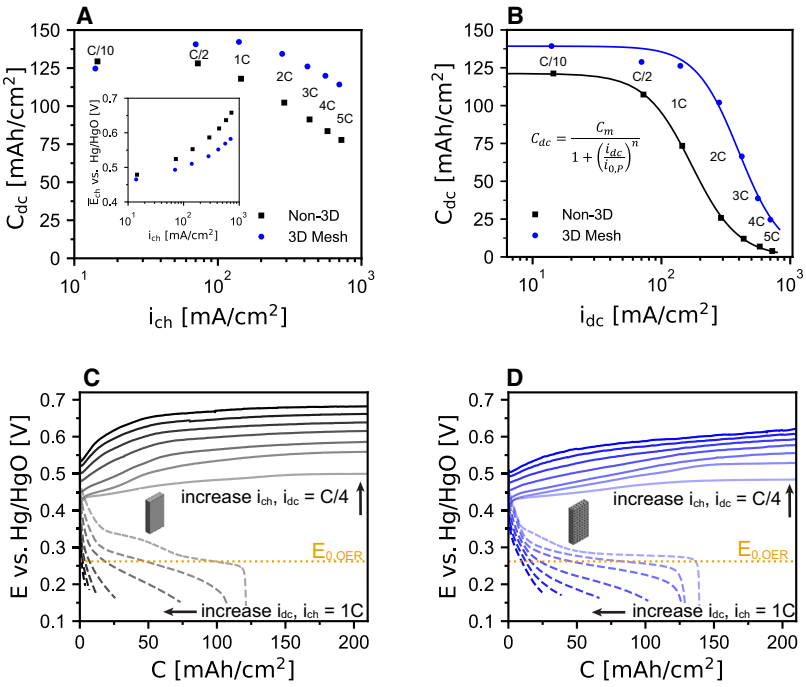

Figure 6. Impact of charge and discharge rate on battery capacity and electrode potential

(A) Experimental areal discharge capacities $C_{A,dc}$ for varying charge rates at 50% overcharge and a C/4 discharge rate. Inset: average charging potential for different charge rates.

(B) Experimental areal discharge capacities $C_{A,dc}$ for varying discharge rates. Electrodes were 50% overcharged at a charge rate of 1 C. Fit based on Peukert equation (Equation 20).

(C and D) Electrode potentials of the non-3D electrode (C) and the 3D mesh electrode (D) for varying charge rates (see A) (solid lines) and discharge rates (see B) (dashed lines).

capacities. For charge rates exceeding 1 C for the non-3D electrode, and 2 C for the 3D electrode, the discharge capacities appear to decrease logarithmically with increased charge rates (Figure 6A). At a total charging time of only 18 min, i.e., a charge rate of 5 C (700 mA/cm^2) and 50% overcharge, the 3D mesh electrode can still provide a specific capacity of 114 mAh/cm^2, which is equivalent to a material utilization of 81.5%. This is 46% higher compared to the non-3D electrode with a material utilization of 54% (78 mAh/cm^2).

Higher current densities result in a shift of CR and OER toward the front of the electrode. This affects the charging efficiency in two ways. First, as discussed above, the more inhomogeneous charging results in an earlier transition to OER at the front of the electrode while the state of charge in the rest of the electrode is still low. Second, the reduced utilization of the electrode's electrochemically active surface area in combination with higher applied current densities results in increased electrode polarization, i.e., overpotentials for both CR and OER. Not only does this result in increased OER, it is also detrimental to the energy efficiency of charging and subsequent electrolysis. The lower ionic resistance of the 3D electrode can compensate for a higher charging current density, thereby facilitating fast charging at a reduced loss in charging efficiency in addition to a reduction in overpotentials (Figures 6A–6D, S17, and S18). This difference in charging potentials increases for higher charge rates and is as high as 100 mV at the 5 C (700 mA/cm^2) charge rate.

As typical for nickel battery electrodes, recharging allows for significantly higher material utilization at elevated current densities than discharging (Figures 6A and 6B).

Table 1. Fit of the generalized Peukert equation

	$i_{0,P}$ (mA/cm^2)	C_m (mAh/cm^2)	n
Non-3D	171	121	2.40
3D mesh	415	134	2.86
CI (non-3D)	[167, 176]	[119, 123]	[2.28, 2.52]
CI (3D mesh)	[381, 450]	[127, 141]	[2.20, 3.52]

Derived from Equation 20. C_m, maximum areal discharge capacity (at C/10 discharge rate, 50% overcharge at 1 C); $i_{0,P}$, discharge current density at which half of C_m is reached; n, exponent of the generalized Peukert equation; CI, confidence interval for the fitted parameters $i_{0,P}$, C_m, and n.

This is because both proton diffusivity and electronic conductivity within the active material film decrease for a lower state of charge.[52] In addition, the discharge starts from the active particles' surface, resulting in a shell with decreased conductivity around the still charged core. Also during discharge, the polarization of the electrolyte results in an inhomogeneously distributed discharging current, which reduces material utilization farther from the electrode surface.[10,22] In addition to electrode kinetics, these effects of inhomogeneous discharging on the scale of the active material thickness (10 μm) and the scale of the electrode thickness (5 mm) determine the relationship between discharge capacity and discharge rate.[10,22] Yazvinskaya et al.[22] introduced a generalized form of the Peukert equation that has been shown to describe this dependence of the discharge capacity on the discharge rate in batteries with nickel positive electrodes:

$$C_{dc} = \frac{C_m}{1+\left(\frac{i_{dc}}{i_{0,P}}\right)^n}. \qquad \text{(Equation 20)}$$

Here, C_m is the maximum discharge capacity the battery can deliver, i_{dc} is the discharge current density, $i_{0,P}$ is the discharge current density at which half of C_m can be extracted, and the exponent n describes the slope of the curve. As shown in Figure 6B, the experimental data can be fit with good agreement to this generalized Peukert equation. The 3D electrode can be discharged around 2.3 times faster than the non-3D electrode and still deliver 50% of the maximum discharge capacity (2.3-fold higher $i_{0,P}$, Table 1) at a current density of 408 mA/cm^2. This is equivalent to an areal capacity of 70 mAh/cm^2 discharged in just 20 min. In contrast, at this current density, only 16 mAh/cm^2 can be discharged from the non-3D electrode. To put these current densities into perspective, the pocket electrodes employed in the previous work reached an areal capacity of approximately 63 mAh/cm^2 at a significantly lower discharge rate of 20 mA/cm^2.[7] However, it is important to note that the discharge current density in a Ni-Fe battery is limited by the iron electrode. Therefore, operating at such high current densities as reached for the 3D nickel electrode discussed here will require further advancements in the rate capability of iron electrodes.[53]

The significant increase in material utilization of the 3D electrode implies that at high discharge current densities the ionic conductivity of the electrode limits the effectively utilized electrode thickness. This is further supported by the results of Lim and Verzwyfelt,[10] who demonstrated that for current densities above 300 mA/cm^2 there is a limiting electrode thickness above which the discharge capacity increases no further. For a discharge current density of 300 mA/cm^2 they report a limiting thickness of 1 mm, which is in agreement with our results for the non-3D electrode. For this reason, sintered electrodes with high rate capability are typically thin, sacrificing energy for power density. Due to the increase in the effective ionic conductivity of the 3D electrode, this limiting value increases by 60% to 1.6 mm.

The discussion above illustrates the drastically improved rate capability of the 3D electrode for both charging and discharging. In addition to the benefits for the hybrid battery-electrolyzer system discussed here, the presented 3D electrodes can contribute to the development of battery energy-storage systems with higher power and energy density (e.g., Ni-Fe, Ni-Cd, Ni-MH, Ni-H_2). Furthermore, the use of thicker electrodes with high areal storage capacity reduces the number of cells required and the associated costs of components such as separators/membranes, connections, and seals.

Electrolysis

After the nickel hybrid electrodes are fully charged, they function as electrolysis electrodes for OER. Sintered nickel electrodes impregnated with nickel hydroxide have been shown in the past to be highly active for oxygen evolution and even outperform noble metal catalysts such as IrO_2.[54,55] To evaluate the impact of the electrode geometry on electrolysis potentials, the non-3D and 3D hybrid electrodes were first fully charged at the 1 C rate for 3 h before undergoing a series of increasing currents for oxygen evolution (Figure 7A). The highest geometric current densities tested were 788 mA/cm^2 and 826 mA/cm^2 for the non-3D and the 3D mesh electrode, respectively. For sufficiently high overpotentials, the relationship between current density and electrode overpotentials can be described by the Tafel relationship $\eta_{OER} = b \log_{10}(i/i_0)$. The Tafel slope b and exchange current density i_0 are determined by fitting the experimental data to the Tafel equation. Generally, a higher exchange current density and lower Tafel slope are characteristic for electrodes with a high activity toward oxygen evolution.[56] The fitted Tafel slopes are almost identical for the non-3D and the 3D electrode with 87 and 90 mV/dec, respectively, but are shifted by the difference in the exchange current density. With respect to the geometric surface area, the exchange current density $i_{0,geo}$ is 4.3×10^{-2} mA/cm^2 for the 3D mesh electrode versus 2.7×10^{-2} mA/cm^2 for the non-3D geometry, which constitutes an increase in activity by a factor of 1.6. At an overpotential of 350 mV, the 3D mesh electrode achieves a current density of 333 mA/cm^2 vs. 285 mA/cm^2 for the non-3D electrode. This is significantly higher than the values reported by Kou et al.[35] (~150 mA/cm^2 at 350 mV), who used a similarly structured 3D-printed nickel electrode loaded with carbon-doped NiO. However, the authors of this study employed a much lower electrolyte concentration compared to our work (1 M vs. ~7.1 M/30 wt % KOH(aq.)). Remarkably, the 3D mesh electrode can provide a higher current even though the channel geometry reduces the electrochemically active surface area by 35% (Figure S5). As a result, the presented 3D mesh electrode could reduce the material costs of the sintered nickel substrate by 44% and still outperform a conventional non-3D electrode. This is especially relevant for upscaling of the technology, as the cost of Ni dominates the electrode material costs and is expected to be in rising demand in the course of the energy transition.[57]

Evaluating the overpotentials with the current normalized to the electrochemically active surface area (ECSA) (Figures 7B and 7C) suggests an apparently higher intrinsic activity of the active material in the 3D electrode (higher i_{ECSA} for a given η_{OER}). However, since both electrodes have been loaded with the same active material, a difference in catalytic activity is excluded. Thus, the differences in electrode polarization must be of structural origin relating to the accessibility, i.e., utilization of active material. To estimate the increase in utilization of the 3D electrode, the Tafel relation can be rewritten as[58]

$$i_{geo} = a_{A,geo}\, i_{0,OER}\, U \exp\left(2.303 \frac{\eta_{OER}}{b}\right), \qquad \text{(Equation 21)}$$

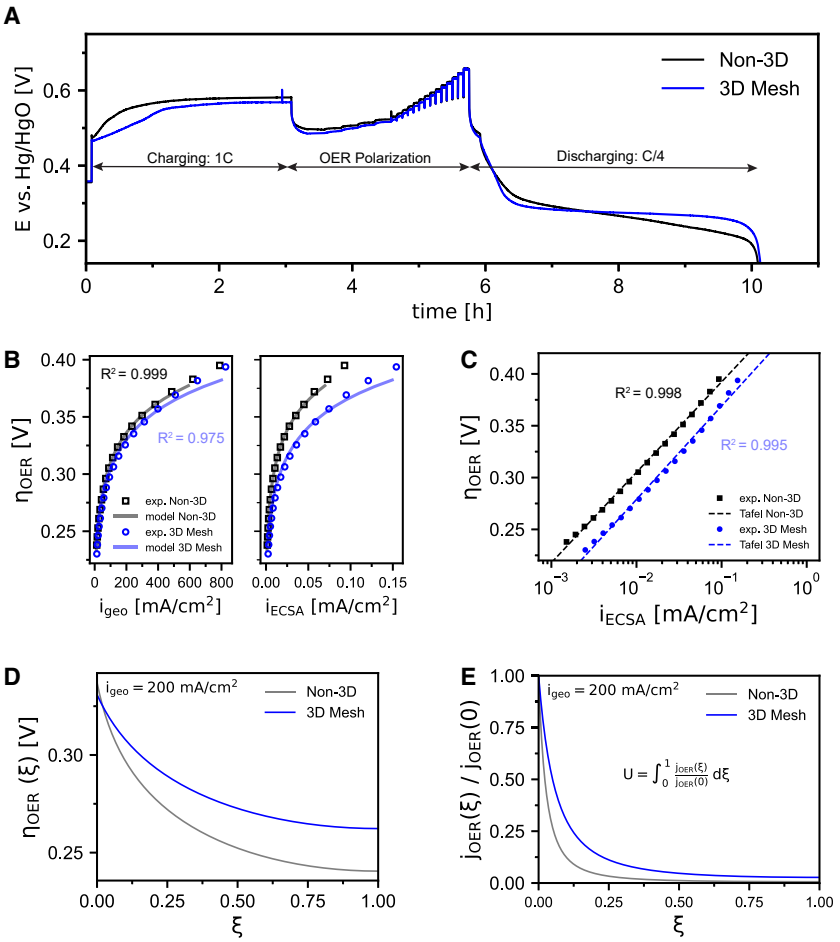

Figure 7. Electrolysis performance

(A) Electrode potential over time during charge (1 C = 140 mA/cm^2), OER polarization experiments, and subsequent discharge (C/4).

(B) Electrode potential vs. geometric current density i_{geo} (left) and vs. current density with respect to the electrochemically active surface area i_{ECSA} (right). The experimental data are compared to the results obtained from the porous-electrode model.

(C) Tafel fit of the oxygen evolution overpotential vs. i_{ECSA}.

(D and E) OER overpotential and current distribution over the reduced electrode thickness $\xi = x/L$ at a geometric current density of 200 mA/cm^2 determined from the porous-electrode model.

where $a_{A,geo}$ is the ECSA per geometric electrode area and U is the utilization. Comparing two electrodes with the same Tafel slope b at a given overpotential, we can write

$$\frac{U_1}{U_2} = \left(\frac{i_{geo,1}}{i_{geo,2}}\right)_{\eta_1 = \eta_2} \frac{a_{A,geo,2}}{a_{A,geo,1}} = \frac{i_{0,ECSA,1}}{i_{0,ECSA,2}}. \quad \text{(Equation 22)}$$

Here, $i_{0,ECSA}$ is the exchange current density with respect to the ECSA (Figure 7C). As the ratio $i_{geo,1}/i_{geo,2}$ at a given overpotential is independent of current density and polarization, the enhancement in utilization is defined by the ratio of the electrodes' respective exchange current densities $i_{0,ECSA}$. Applying Equation 22 to our experimental data results in an estimated 2.5-fold increase in utilization of the 3D electrode. As discussed for the 3D electrode's improved charging efficiency and (dis) charge rate capabilities, the observed increase in utilization can be explained with the lower effective ionic electrode resistance of the more open 3D structure. This

results in a reduced gradient in overpotential across the electrode thickness and, thus, a more homogeneous current distribution as determined with the porous-electrode model (Figure S6). Using said current distribution, the utilization can be determined as

$$U = \int_0^1 \frac{j_{OER}(\xi)}{j_{OER}(0)} d\xi, \qquad \text{(Equation 23)}$$

where $j_{OER}(\xi)$ is the local OER current density at the reduced position $\xi = x/L$, and $j_{OER}(0)$ is the current density at the electrode front facing the counter electrode. For an applied current density of 200 mA/cm^2, the utilization is calculated as 5.3% and 12.1% for the non-3D and 3D electrode, respectively. Remarkably, the utilization enhancement calculated with the simple model is only marginally lower than that determined experimentally (2.2 vs. 2.5). Such low utilization as the consequence of the high ionic voltage drop is the reason why the thickness of porous electrodes or active coatings is typically well below 1 mm for electrolysis.[54,55,58] While increasing the electrode thickness increases the ECSA, there is a limit above which any additional ECSA is not utilized due to the increasingly high ionic resistance. This limit is also known as the reaction penetration depth.[59,60] Electrodes thicker than the reaction penetration depth do not increase the effectively utilized ECSA so that electrode polarization does not decrease either. With regard to the 3D electrode discussed in this work, this poses an interesting optimization question. While a more open geometry with a high void fraction θ increases the effective ionic electrode conductivity and electrode utilization, the total ECSA is reduced by a factor $(1 - \theta)$. This implies that there must be an optimal electrode void fraction for each current density that maximizes the ionically accessible ECSA and thus minimizes electrode polarization for a given thickness and porosity.

We note that even if OER utilization is low for the hybrid electrodes discussed here, most of the electrode is utilized for the battery (dis)charging reaction (Figures 5 and 6). As stated above, this is because at low $S(q)$ the exchange current density for charging is many orders of magnitude larger than for OER. Therefore, 3D hybrid battery-electrolysis electrodes will generally be thicker than dedicated electrolysis electrodes and will still be able to charge the full thickness.

In the discussion above we have not yet considered the possible effect of bubbles on electrode utilization. Bubbles flooding the pores and adhering to the electrode surface are known to cover electrochemically active sites[25,61] and reduce the effective electrolyte conductivity,[62,63] resulting in a decrease in electrode utilization.[54,55,58] Appleby et al.[55] demonstrated that only around 40% of the ECSA is utilized for OER (extrapolated by Hall[54]) for a 0.15-mm-thick sintered nickel electrode. For such thin electrodes, where the ionic resistance is not limiting, a reduction in utilization can be attributed clearly to the adverse effects of bubbles within the pores. However, our results suggest that any adverse effects of bubbles on the utilization are small compared to the impact of the effective ionic conductivity. First, the simple electrode model appears to describe the overpotentials and utilization enhancement for the tested electrodes reasonably well (Figures 5 and S6), even without taking bubbles into account. Second, if we assume that only 40%[54,55] of the OER generating ECSA is available due to bubble coverage (for example at 200 mA/cm^2), that would decrease the utilization of the non-3D electrode further from 5.3% to 2.12%, which is not observed. Therefore, it is clear that in this work the main mechanism by which the 3D electrode increases electrode utilization is by increasing the effective ionic conductivity of the electrode. Interestingly, the

experimental data can be fitted using a simple Tafel relation with a current-independent slope *b* (Figure 6C). This implies that the bubble coverage is not yet leading to additional transport resistances at these current densities, as has also been shown in earlier studies on sintered nickel electrodes for both OER[54,55] and HER.[58]

While the measured performance gain of the 3D electrode can be mostly attributed to an improved ionic conductivity into the porous electrode, one may expect additional advantages on current densities in a full electrolyzer cell, where such an electrode can be configured in a zero-gap flow-through configuration. The electrolyte flowing through, rather than past, the electrode improves not only bubble removal but could also facilitate mass and heat transfer.[36,64–67] The latter is especially relevant at high current densities, whereby overheating can result in decreased battery cycling stability and charging efficiency.[12,13,68]

Energy efficiency

To put the reduction in overpotentials and the increased areal capacity into perspective for the practical application as an integrated battery-electrolyzer, we can estimate the overall energy efficiency for a full cell[7]:

$$\eta_{tot} = \frac{C_{dc}(\overline{E}_{Ni,dc} - \overline{E}_{Fe,dc} - \eta_{\Omega,dc}) + 1.48\ V(C_{cr} - C_{dc})}{C_{cr}(\overline{E}_{Ni,cr} - \overline{E}_{Fe,cr} + \eta_{\Omega,cr})}. \qquad \text{(Equation 24)}$$

Here, $\overline{E}_{Ni}$ and $\overline{E}_{Fe}$ represent the average observed potentials during charge (cr) and discharge (dc) of the nickel and iron electrode, respectively. Ionic overpotentials induced by the electrolyte resistivity in the interelectrode gap are denoted as η_{Ω}. Specifically for charging and electrolysis, this resistivity may be increased by some screening effect of bubbles.[24,69] The energy that can be stored and extracted from the cell consists of the energy retrieved during discharging of the battery determined by the average discharging potentials of anode and cathode. In addition, the energy stored in the form of hydrogen is determined from the thermoneutral voltage for alkaline water electrolysis (1.48 V, the difference of E_{TN}(OER) = 0.565 V and E_{TN}(HER) = −0.912 V vs. Hg/HgO, see Note S3), while the charge insertion for electrolysis is estimated from the difference between inserted charge and discharge capacity. Here we assume that the battery is cycled from fully discharged, to charged and fully discharged, and the missing charge is converted to H_2 and O_2 either during discharge (or eventually due to self-discharge when idling after charge). In this work, the discussed nickel electrodes were only cycled individually and not in a full cell paired with an iron electrode. Therefore, we estimate the total energy efficiency with data from a non-3D sintered iron electrode that had been operated at similar charging/discharging current densities and charge insertion (see Figure S7). The ohmic potential drop between the electrodes is dependent on the exact cell configuration to be used. Here only the electrolyte resistance in an assumed electrode gap of 1.5 mm is used. Effects of bubbles on the electrolyte resistance and a membrane resistance are not taken into account, as the current densities are limited. The total energy efficiency was calculated for a charge rate of 1 C and a discharge rate of C/4, which is equivalent to a charging/discharging current density of 145 mA/cm^2/36 mA/cm^2 for the non-3D electrode and 140 mA/cm^2/35 mA/cm^2 for the 3D mesh electrode. The electrodes were overcharged to 6 C. This results in an estimated total energy efficiency of 76.4% and 78.9% for the non-3D and 3D mesh electrode at room temperature, respectively.

It is worth noting that similar benefits in overpotential and capacity utilization are to be expected from a sintered iron electrode with comparable 3D structure.

In addition, the efficiency can be increased further by operating the cell at higher temperatures. This reduces activation overpotentials and increases the conductivity of the electrolyte.

In total, the electrode tests including charge, discharge, and electrolysis at different rates lasted for up to 345 h, with 627 h of discharging during more than 150 cycles (Figure S8). The electrodes maintain capacity and rate performance, although some $Ni(OH)_2$ directly on the surface has detached, as is observed in X-ray diffraction of the electrode surface (Figure S9).

EXPERIMENTAL PROCEDURES

Chemicals

Nickel powder (−325 mesh, <53 μm, 99.8%), potassium hydroxide (85%), nickel(II) nitrate hexahydrate (98%), and carboxymethylcellulose sodium salt (CMC) were purchased from Alfa Aesar. Araldite two-component epoxy resin was purchased from RS Components. Ultrapure water was prepared using a Merck Milli-Q Plus 185. The H_2/Ar mixture (5%:95%) was purchased from Linde. The resin used with the Formlabs Form-2 stereolithographic (SLA) 3D printer ("Clear" resin) was purchased from MakerPoint. The 3D electrode molds were 3D printed from the PLA filament "EasyFil PLA" purchased from Form Futura.

Electrode preparation

Electrode molds and filling tools were designed using the CAD software Autodesk Inventor 2019. The electrode molds were then printed in PLA via FDM on a Prusa MK3 S 3D printer. Filling tools used to inject the paste into the 3D electrode molds were printed in clear resin on a Formlabs Form-2 SLA 3D printer. Using the filling tools and a 5-mL syringe with luer-lock connection, the electrode molds were filled with a nickel paste consisting of nickel powder (61.5 wt %), epoxy (14.3 wt %), and an aqueous solution of 3 wt % carboxymethylcellulose sodium salt (24.2 wt %). The ratios of the paste compounds are based on the findings of Hereijgers et al.[30]

Before the removal of the electrode mold, solidifying the electrode paste is required by curing the epoxy resin at 60°C for 3 h. Following the curing procedure, excess hardened paste is filed off from the mold openings with a powered filing tool (Dremel). This is essential to prevent blockage of the channels in the final electrode. After curing of the epoxy, the PLA mold material was removed by placing the molds in well-stirred 25 wt % aqueous potassium hydroxide solution at 80°C for 15 h. This results in the dissolution of most of the mold material. Any remaining PLA is softened sufficiently to be blown off with pressurized nitrogen. The epoxy, and thus the mechanical integrity of the green part, was not affected by the potassium hydroxide solution. Following the mold removal, the green parts were rinsed thoroughly in demineralized water in order to remove the potassium hydroxide. Finally, the green parts were dried at 80°C under vacuum (100 mbar) to constant weight (Thermo Scientific VT 6025 vacuum drying oven).

In the next step, the rinsed green parts are sintered in a furnace under atmospheric conditions (Nabertherm L5/12/C450). We adapted the sintering procedure from Hereijgers et al.[30] Under atmospheric conditions, the green part is first heated to 350°C (5°C min^{-1}), followed by a temperature increase to 600°C (1°C min^{-1}). The green part is kept at 600°C for 1 h to burn away the epoxy before increasing the temperature to 1,000°C (1°C min^{-1}). Sintering of the metal particles is achieved by maintaining the temperature at 1,000°C for 1 h followed by cooling down to room temperature at a rate of 5°C min^{-1}. This initial sintering step must be conducted in

the presence of oxygen, i.e., atmospheric conditions, to fully burn out the epoxy resin and any PLA residues. Under an inert argon atmosphere, i.e., pyrolysis conditions, Hereijgers et al.[30] report carbon residues from the epoxy resin that prevent the sintering of the nickel particles. However, this results in the oxidation of the nickel structure, significantly reducing the electrical conductivity. Therefore, a second sintering step under a reducing atmosphere (H_2/Ar) is necessary. The brown parts were transferred to a tube oven (Applied Test Systems, Series 3210) with a quartz tube of 35 mm in diameter. Air was removed by evacuating and refilling the tube with a mixture of 5% H_2 in Ar three times. The temperature was increased to 800°C (1°C min^{-1}) and held for 2 h at a flow rate of 100 mL min^{-1}. This allows for the complete reduction of nickel oxide formed in the brown part during the initial sintering step under atmosphere. The degree of reduction is assessed via the weight decrease of the electrode (~21% decrease in weight from NiO to Ni) as well as via X-ray diffraction. During the sintering procedure the electrodes shrink, as summarized in Table S1. We observe further that temperature inhomogeneities induced by the gas flow in the tube oven can result in warpage of the electrodes. This warpage is more likely to occur for the non-3D electrodes, as the open structure of the 3D electrodes facilitates a more homogeneous temperature profile. Nickel contacts (0.15 mm thick) were purchased from NKON and spot-welded onto the sides of the electrode with a SUNKKO 738 AL spot-welding machine purchased from Banggood. Prior to spot welding, the electrodes were cleaned with acetone using ultrasound for 5 min, followed by drying at 80°C under vacuum (100 mbar) to constant weight.

Nickel hydroxide ($Ni(OH)_2$) was loaded on the reduced electrodes by thermal decomposition of nickel(II) nitrate hexahydrate ($Ni(NO_3)_2 \cdot 6H_2O$) based on the procedure outlined by Falk and Salkind[21] (Figure S3). Nickel nitrate hexahydrate (~200 g) was placed in an SAN container (500 mL, Mepal) and placed in a preheated vacuum oven at 100°C. As soon as the nitrate bath has reached a temperature of approximately 90°C, the electrodes were placed in the molten nickel nitrate hexahydrate and vacuum (40 mbar) applied for 4 min followed by 6 min under atmospheric conditions. Note that no additional water was added. The electrodes were then removed from the nickel nitrate bath and excess material on the electrode surface blown off with nitrogen. In the next step, the now loaded electrodes were roasted in a furnace at 220°C for 1 h under atmosphere. The electrodes were then removed from the oven and excess material once again brushed off from the electrode surface. Special care has to be taken to remove material that has accumulated within the open structures of the electrodes. In the next step, the electrodes were placed in 25 wt % aqueous potassium hydroxide solution at 80°C overnight. This was followed by a rigorous rinsing step in demineralized water at 80°C to remove remaining nitrates. The loaded electrodes were then dried at 80°C under vacuum (100 mbar) to constant weight. This loading procedure was repeated four times to reach the desired theoretical capacity of ~140 mAh/cm^2 (based on 289 mAh/g of $Ni(OH)_2$). We note that it is essential to spot weld the contacts before the loading procedure.

Electrochemical testing

The electrodes were placed in a 3D-printed frame as shown in Figure S11. The frame was designed in Autodesk Inventor 2019 and printed with a Formlabs Form-2 stereolithographic 3D printer using Formlabs' proprietary "Clear" resin. This allows for the secure and reproducible positioning of the reference electrode (RE), counter electrode (CE, Ni foam), and working electrode (WE). The Hg/HgO RE (Origalys Origasens) was placed adjacent to the WE and connected ionically

via a capillary. Due to the vicinity of the RE to the WE, the required voltage correction due to the solution resistance is reduced. A groove in the frame allows for bubbles to escape between the electrode contact and capillary so that noise in the potential measurement (WE vs. RE) is significantly reduced. One of the two welded electrode contacts was used to insert the current, and the other was used to measure the electrode potential. This removes the electronic resistance of the nickel strip as well as the contact resistance from the measurement. Note that a CE was installed on either side of the WE, but for all data shown in this work only one CE was connected. Furthermore, a thermocouple (RS PRO Type T, 1.5 mm diameter, purchased from RS Online) was placed next to the WE. This was included to ensure that temperatures do not rise excessively, especially at high current densities. The frame including the WE, RE, CE, and thermocouple was placed in a 500-mL SAN container (Mepal) filled with approximately 450 g of 30 wt % KOH(aq.). Contacts, RE, and thermocouple were led through openings cut in the lid and secured with Parafilm (Figure S12). All experiments involving battery cycling, i.e., charging and discharging, were conducted with a Maccor 4000 battery cycling system. Electrochemical impedance spectroscopy (EIS) and ECSA measurements were conducted using a PARSTAT 4000A potentiostat (Princeton Applied Research) (Figures S5 and S13). If not stated otherwise, all reported voltages have been iR-corrected via the solution resistance measured via EIS (Figure S13). Water consumed during electrolysis was replaced regularly with ultrapure water to minimize changes in electrolyte concentration. The potential of the used Hg/HgO reference electrodes vs. the reversible hydrogen electrode (RHE) was determined using a HydroFlex RHE purchased from Gaskatel.

RESOURCE AVAILABILITY

Lead contact

Further information and requests for resources should be directed to the lead contact, F.M. Mulder (f.m.mulder@tudelft.nl).

Materials availability

This study did not generate new unique materials. For a more detailed explanation on the manufacturing procedure of the 3D electrodes, we refer readers to the supplemental information.

Data and code availability

The datasets generated during this study will be available in a repository with https://doi.org/10.4121/a87a59f5-e43a-4527-b047-dd6fb766b31b. Any questions will be handled by the lead contact upon reasonable request.

ACKNOWLEDGMENTS

This work is part of the Open Technology Research Program with project number 15169, which is (partly) financed by The Netherlands Organization for Scientific Research (NWO). We thank Loebna Akkouh and Jeannet Liang for their contribution to the optimization of the experimental protocol for the fabrication of indirectly 3D-printed nickel electrodes.

AUTHOR CONTRIBUTIONS

Conceptualization, R.M.-G. and F.M.M.; experimental investigations and porous model development and implementation, R.M.-G.; methodology, R.M.-G. and F.M.M.; writing, review, and editing, R.M.-G. and F.M.M.; project funding and initiation, F.M.M.

DECLARATION OF INTERESTS

A patent was submitted based on the current work. F.M.M. is co-founder of Battolyser Systems, a TU Delft spin-off company for the commercialization of Battolyser™ technology.

SUPPLEMENTAL INFORMATION

Supplemental information can be found online at https://doi.org/10.1016/j.xcrp.2024.102286.

Received: March 1, 2024
Revised: April 23, 2024
Accepted: October 17, 2024
Published: November 20, 2024

REFERENCES

1. Pörtner, H.-O., Roberts, D.C., Adams, H., Adler, C., Aldunce, P., Ali, E., Begum, R.A., Betts, R., Kerr, R.B., and Biesbroek, R. (2022). Climate Change 2022: Impacts, Adaptation and Vulnerability. IPCC Sixth Assessment Report.

2. Kemp, L., Xu, C., Depledge, J., Ebi, K.L., Gibbins, G., Kohler, T.A., Rockström, J., Scheffer, M., Schellnhuber, H.J., Steffen, W., and Lenton, T.M. (2022). Climate Endgame: Exploring catastrophic climate change scenarios. Proc. Natl. Acad. Sci. USA *119*, e2108146119. https://doi.org/10.1073/pnas.2108146119.

3. Hoegh-Guldberg, O., Jacob, D., Taylor, M., Guillén Bolaños, T., Bindi, M., Brown, S., Camilloni, I.A., Diedhiou, A., Djalante, R., Ebi, K., et al. (2019). The human imperative of stabilizing global climate change at 1.5°C. Science *365*, eaaw6974. https://doi.org/10.1126/science.aaw6974.

4. Mulder, F.M. (2014). Implications of diurnal and seasonal variations in renewable energy generation for large scale energy storage. J. Renew. Sustain. Energy *6*, 033105. https://doi.org/10.1063/1.4874845.

5. Blair, N., Augustine, C., Cole, W., Denholm, P., Frazier, W., Geocaris, M., Jorgenson, J., McCabe, K., Podkaminer, K., Prasanna, A., et al. (2022). Storage Futures Study: Key Learnings for the Coming Decades (NREL). https://www.nrel.gov/docs/fy22osti/81779.pdf.

6. Palys, M.J., and Daoutidis, P. (2020). Using hydrogen and ammonia for renewable energy storage: A geographically comprehensive techno-economic study. Comput. Chem. Eng. *136*, 106785. https://doi.org/10.1016/j.compchemeng.2020.106785.

7. Mulder, F.M., Weninger, B.M.H., Middelkoop, J., Ooms, F.G.B., and Schreuders, H. (2017). Efficient electricity storage with a battolyser, an integrated Ni–Fe battery and electrolyser. Energy Environ. Sci. *10*, 756–764. https://doi.org/10.1039/C6EE02923J.

8. Shukla, A.K., Ravikumar, M.K., and Balasubramanian, T.S. (1994). Nickel/iron batteries. J. Power Sources *51*, 29–36. https://doi.org/10.1016/0378-7753(94)01953-3.

9. Abarro, J.M.E., Gavan, J.N.L., Loresca, D.E.D., Ortega, M.A.A., Esparcia, E.A., Jr., and Paraggua, J.A.D.R. (2023). A tale of nickel-iron batteries: Its resurgence in the age of modern batteries. Batteries *9*, 383.

10. Lim, H.S., and Verzwyvelt, S.A. (1996). Effects of electrode thickness on power capability of a sintered-type nickel electrode. J. Power Sources *62*, 41–44. https://doi.org/10.1016/S0378-7753(96)02404-4.

11. Manohar, A.K., Yang, C., Malkhandi, S., Prakash, G.K.S., and Narayanan, S.R. (2013). Enhancing the performance of the rechargeable iron electrode in alkaline batteries with bismuth oxide and iron sulfide additives. J. Electrochem. Soc. *160*, A2078–A2084.

12. Oshitani, M., Sasaki, Y., and Takashima, K. (1984). Development of a nickel electrode having stable performance at various charge and discharge rates over a wide temperature range. J. Power Sources *12*, 219–231. https://doi.org/10.1016/0378-7753(84)80021-X.

13. Li, J., Shangguan, E., Guo, D., Li, Q., Chang, Z., Yuan, X.-Z., and Wang, H. (2014). Calcium metaborate as a cathode additive to improve the high-temperature properties of nickel hydroxide electrodes for nickel–metal hydride batteries. J. Power Sources *263*, 110–117. https://doi.org/10.1016/j.jpowsour.2014.03.134.

14. Sui, Y., and Ji, X. (2021). Anticatalytic strategies to suppress water electrolysis in aqueous batteries. Chem. Rev. *121*, 6654–6695.

15. Iranzo, A., and Mulder, F.M. (2021). Nickel-iron layered double hydroxides for an improved Ni/Fe hybrid battery-electrolyser. Mater. Adv. *2*, 5076–5088. https://doi.org/10.1039/D1MA00024A.

16. Holst, M., Aschbrenner, S., Smolinka, T., Voglstätter, C., and Grimm, G. (2021). Cost forecast for low temperature electrolysis-technology driven bottom-up prognosis for PEM and alkaline water electrolysis systems.

17. van't Noordende, H., and Ripson, P. (2020). A one-GigaWatt green-hydrogen plant, advanced design and total installed capital costs.

18. Haverkort, J.W., and Rajaei, H. (2021). Voltage losses in zero-gap alkaline water electrolysis. J. Power Sources *497*, 229864. https://doi.org/10.1016/j.jpowsour.2021.229864.

19. Lira Garcia Barros, R., Kraakman, J.T., Sebregts, C., van der Schaaf, J., and de Groot, M.T. (2024). Impact of an electrode-diaphragm gap on diffusive hydrogen crossover in alkaline water electrolysis. Int. J. Hydrogen Energy *49*, 886–896. https://doi.org/10.1016/j.ijhydene.2023.09.280.

20. TenneT (2023). TenneT Adequacy Outlook 2023.

21. Falk, S.U., and Salkind, A.J. (1969). Alkaline storage batteries.

22. Yazvinskaya, N.N., Galushkin, N.E., Galushkin, D.N., and Kalmykov, B.Y. (2020). Analysis and comparison of generalized Peukert's equations parameters for nickel-cadmium batteries with pocket and sintered electrodes. Int. J. Electrochem. Sci. *15*, 412–423.

23. Chandrasekaran, S., Lin, D., Li, Y., and Worsley, M.A. (2023). Aerogels, additive manufacturing, and energy storage. Joule *7*, 866–883. https://doi.org/10.1016/j.joule.2023.03.021.

24. Wosiak, G., Silva, J.d., Sena, S.S., Carneiro-Neto, E.B., Lopes, M.C., and Pereira, E. (2022). Investigation of the influence of the void fraction on the energy consumption of a vertical electrolyser under natural convection. J. Environ. Chem. Eng. *10*, 107577. https://doi.org/10.1016/j.jece.2022.107577.

25. Vogt, H. (2012). The actual current density of gas-evolving electrodes—Notes on the bubble coverage. Electrochim. Acta *5*.

26. Mooraj, S., Qi, Z., Zhu, C., Ren, J., Peng, S., Liu, L., Zhang, S., Feng, S., Kong, F., Liu, Y., et al. (2020). 3D printing of metal-based materials for renewable energy applications. Nano Res. *14*, 2105–2132. https://doi.org/10.1007/s12274-020-3230-x.

27. Xu, X., Tan, Y.H., Ding, J., Guan, C., and Guan, C. (2021). 3D Printing of Next-generation Electrochemical Energy Storage Devices: from Multiscale to Multimaterial. Energy &. Environ. Materials *5*, 427–438. https://doi.org/10.1002/eem2.12175.

28. Zeng, L., Li, P., Yao, Y., Niu, B., Niu, S., Xu, B., and Xu, B. (2020). Recent progresses of 3D printing technologies for structural energy storage devices. Materials Today Nano *12*, 100094. https://doi.org/10.1016/j.mtnano.2020.100094.

29. Arenas, L.F., Ponce de León, C., and Walsh, F.C. (2017). 3D-printed porous electrodes for advanced electrochemical flow reactors: A Ni/stainless steel electrode and its mass transport characteristics. Electrochem. Commun. *77*, 133–137. https://doi.org/10.1016/j.elecom.2017.03.009.

30. Hereijgers, J., Schalck, J., Lölsberg, J., Wessling, M., and Breugelmans, T. (2019). Indirect 3D Printed Electrode Mixers. ChemElectroChem *6*, 378–382. https://doi.org/10.1002/celc.201801436.

31. Hereijgers, J., Schalck, J., and Breugelmans, T. (2020). Mass transfer and hydrodynamic characterization of structured 3D electrodes for electrochemistry. Chem. Eng. J. *384*, 123283. https://doi.org/10.1016/j.cej.2019.123283.

32. Lölsberg, J., Starck, O., Stiefel, S., Hereijgers, J., Breugelmans, T., and Wessling, M. (2017). 3D-Printed Electrodes with Improved Mass Transport Properties. ChemElectroChem *4*, 3309–3313. https://doi.org/10.1002/celc.201700662.

33. Beck, V.A., Ivanovskaya, A.N., Chandrasekaran, S., Forien, J.-B., Baker, S.E., Duoss, E.B., and

Worsley, M.A. (2021). Inertially enhanced mass transport using 3D-printed porous flow-through electrodes with periodic lattice structures. Proc. Natl. Acad. Sci. USA *118*, e2025562118. https://doi.org/10.1073/pnas.2025562118.

34. Bui, J.C., Davis, J.T., Esposito, D.V., and Esposito, D.V. (2020). 3D-Printed electrodes for membraneless water electrolysis. Sustain. Energy Fuels *4*, 213–225. https://doi.org/10.1039/c9se00710e.

35. Kou, T., Wang, S., Shi, R., Zhang, T., Chiovoloni, S., Lu, J.Q., Chen, W., Worsley, M.A., Wood, B.C., Baker, S.E., et al. (2020). Periodic Porous 3D Electrodes Mitigate Gas Bubble Traffic during Alkaline Water Electrolysis at High Current Densities. Adv. Energy Mater. *10*, 2002955. https://doi.org/10.1002/aenm.202002955.

36. Sullivan, I., Zhang, H., Zhu, C., Wood, M., Nelson, A.J., Baker, S.E., Spadaccini, C.M., van Buuren, T., Lin, M., Duoss, E.B., et al. (2021). 3D Printed Nickel-Molybdenum-Based Electrocatalysts for Hydrogen Evolution at Low Overpotentials in a Flow-Through Configuration. ACS Appl. Mater. Interfaces *13*, 20260–20268. https://doi.org/10.1021/acsami.1c05648.

37. Saleh, M.S., Li, J., Park, J., and Panat, R. (2018). 3D printed hierarchically-porous microlattice electrode materials for exceptionally high specific capacity and areal capacity lithium ion batteries. Addit. Manuf. *23*, 70–78. https://doi.org/10.1016/j.addma.2018.07.006.

38. Lyu, Z., Lim, G.J., Koh, J.J., Li, Y., Ma, Y., Ding, J., Wang, J., Hu, Z., Wang, J., Chen, W., and Chen, Y. (2021). Design and Manufacture of 3D-Printed Batteries. Joule *5*, 89–114. https://doi.org/10.1016/j.joule.2020.11.010.

39. Kong, D., Wang, Y., Huang, S., Zhang, B., Lim, Y.V., Sim, G.J., Valdivia Y Alvarado, P., Ge, Q., Yang, H.Y., and Yang, H.Y. (2020). 3D Printed Compressible Quasi-Solid-State Nickel-Iron Battery. ACS Nano *14*, 9675–9686. https://doi.org/10.1021/acsnano.0c01157.

40. Li, C., Du, J., Gao, Y., Bu, F., Tan, Y.H., Wang, Y., Fu, G., Guan, C., Xu, X., and Huang, W. (2022). Stereolithography of 3D sustainable metal electrodes towards high-performance nickel iron battery. Adv. Funct. Mater. *32*, 2205317.

41. Roy, T., Salazar de Troya, M.A., Worsley, M.A., and Beck, V.A. (2022). Topology optimization for the design of porous electrodes. Struct. Multidiscip. Optim. *65*, 171. https://doi.org/10.1007/s00158-022-03249-2.

42. Danninger, H., Calderon, R., and Gierl-Mayer, C. (2017). Powder metallurgy and sintered materials. Addit. Manuf. *19*.

43. Chung, S.-H., Kwon, Y.-S., Hyun, C.-M., Kim, K., Kim, M.-J., and German, R.M. (2004). Analysis and design of a press and sinter process for fabrication of precise tungsten carbide cutting tools. Advances in Powder Metallurgy and Particulate Materials. Partisans *8*, 8–26.

44. Dehghan-Manshadi, A., Yu, P., Dargusch, M., StJohn, D., and Qian, M. (2020). Metal injection moulding of surgical tools, biomaterials and medical devices: A review. Powder Technol. *364*, 189–204. https://doi.org/10.1016/j.powtec.2020.01.073.

45. Posey, F.A. (1964). Methods for the Calculation of Polarization in Porous Electrodes. J. Electrochem. Soc. *111*, 1173. https://doi.org/10.1149/1.2425944.

46. Ta, K.P., and Newman, J. (1998). Mass Transfer and Kinetic Phenomena at the Nickel Hydroxide Electrode. J. Electrochem. Soc. *145*, 3860–3874. https://doi.org/10.1149/1.1838886.

47. De Vidts, P., and White, R.E. (1995). Mathematical Modeling of a Nickel-Cadmium Cell: Proton Diffusion in the Nickel Electrode. J. Electrochem. Soc. *142*, 1509–1519. https://doi.org/10.1149/1.2048605.

48. Fan, D., and White, R.E. (1991). Mathematical Modeling of a Nickel-Cadmium Battery Effects of Intercalation and Oxygen Reactions. J. Electrochem. Soc. *138*, 2952–2960. https://doi.org/10.1149/1.2085347.

49. Tuomi, D. (1965). The Forming Process in Nickel Positive Electrodes. J. Electrochem. Soc. *112*, 1. https://doi.org/10.1149/1.2423457.

50. Zimmerman, A.H. (1984). Technological implications in studies of nickel electrode performance and degradation. J. Power Sources *12*, 233–245. https://doi.org/10.1016/0378-7753(84)80022-1.

51. Yuan, A., Cheng, S., Zhang, J., and Cao, C. (1998). The influence of calcium compounds on the behaviour of the nickel electrode. J. Power Sources *76*, 36–40. https://doi.org/10.1016/s0378-7753(98)00130-x.

52. Motupally, S., Streinz, C.C., and Weidner, J.W. (1998). Proton Diffusion in Nickel Hydroxide: Prediction of Active Material Utilization. J. Electrochem. Soc. *145*, 29–34. https://doi.org/10.1149/1.1838205.

53. Manohar, A.K., Malkhandi, S., Yang, B., Yang, C., Surya Prakash, G.K., and Narayanan, S.R. (2012). A High-Performance Rechargeable Iron Electrode for Large-Scale Battery-Based Energy Storage. J. Electrochem. Soc. *159*, A1209–A1214. https://doi.org/10.1149/2.034208jes.

54. Hall, D.E. (1983). $Ni(OH)_2$-Impregnated Anodes for Alkaline Water Electrolysis. J. Electrochem. Soc. *130*, 317–321. https://doi.org/10.1149/1.2119702.

55. Appleby, A., Crepy, G., and Jacquelin, J. (1978). High efficiency water electrolysis in alkaline solution. Int. J. Hydrogen Energy *3*, 21–37. https://doi.org/10.1016/0360-3199(78)90054-X.

56. Zeng, K., and Zhang, D. (2010). Recent progress in alkaline water electrolysis for hydrogen production and applications. Prog. Energy Combust. Sci. *36*, 307–326. https://doi.org/10.1016/j.pecs.2009.11.002.

57. Boer, L., Pescatori, M.A., and Stuermer, M. (2021). Energy Transition Metals (International Monetary Fund).

58. Rausch, S., and Wendt, H. (1996). Morphology and utilization of smooth hydrogen-evolving Raney nickel cathode coatings and porous sintered-nickel cathodes. J. Electrochem. Soc. *143*, 2852–2862. https://doi.org/10.1149/1.1837118.

59. Kadyk, T., Bruce, D., and Eikerling, M. (2016). How to Enhance Gas Removal from Porous Electrodes. Sci. Rep. *6*, 38780. https://doi.org/10.1038/srep38780.

60. Liu, M.-B., Cook, G.M., and Yao, N.P. (1982). Transient current distributions in porous zinc electrodes in KOH electrolyte. J. Electrochem. Soc. *129*, 239–246.

61. Lake, J.R., Soto, Á.M., and Varanasi, K.K. (2022). Impact of Bubbles on Electrochemically Active Surface Area of Microtextured Gas-Evolving Electrodes. Langmuir *38*, 3276–3283. https://doi.org/10.1021/acs.langmuir.2c00035.

62. Abdelghani-Idrissi, S., Dubouis, N., Grimaud, A., Stevens, P., Toussaint, G., and Colin, A. (2021). Effect of electrolyte flow on a gas evolution electrode. Sci. Rep. *11*, 4677. https://doi.org/10.1038/s41598-021-84084-1.

63. Ateya, B.G., and El-Anadouli, B.E. (1991). Effects of Gas Bubbles on the Polarization Behavior of Porous Flow Through Electrodes. J. Electrochem. Soc. *138*, 1331–1336. https://doi.org/10.1149/1.2085781.

64. Eigeldinger, J., and Vogt, H. (2000). The bubble coverage of gas-evolving electrodes in a flowing electrolyte. Electrochim. Acta *45*, 4449–4456. https://doi.org/10.1016/s0013-4686(00)00513-2.

65. Balzer, R.J., and Vogt, H. (2003). Effect of Electrolyte Flow on the Bubble Coverage of Vertical Gas-Evolving Electrodes. J. Electrochem. Soc. *150*, E11. https://doi.org/10.1149/1.1524185.

66. Rocha, F., Delmelle, R., Georgiadis, C., and Proost, J. (2022). Effect of pore size and electrolyte flow rate on the bubble removal efficiency of 3D pure Ni foam electrodes during alkaline water electrolysis. J. Environ. Chem. Eng. *10*, 107648. https://doi.org/10.1016/j.jece.2022.107648.

67. de Radiguès, Q., Thunis, G., and Proost, J. (2019). On the use of 3-D electrodes and pulsed voltage for the process intensification of alkaline water electrolysis. Int. J. Hydrogen Energy *44*, 29432–29440. https://doi.org/10.1016/j.ijhydene.2019.06.156.

68. Fierro, C., Zallen, A., Fierro, C., Koch, J., Koch, J., Fetcenko, M.A., Fetcenko, M.A., and Fetcenko, M.A. (2006). The Influence of Nickel-Hydroxide Composition and Microstructure on the High-Temperature Performance of Nickel Metal Hydride Batteries. J. Electrochem. Soc. *153*, A492. https://doi.org/10.1149/1.2161577.

69. Bongenaar-Schlenter, B.E., Janssen, L.J.J., Van Stralen, S.J.D., and Barendrecht, E. (1985). The effect of the gas void distribution on the ohmic resistance during water electrolytes. J. Appl. Electrochem. *15*, 537–548. https://doi.org/10.1007/BF01059295.